

Control of magnetic properties of MnBi_2Te_4 using a van der Waals ferroelectric $\text{III}_2\text{-VI}_3$ film and biaxial strain

Feng Xue,^{1,*} Zhe Wang,^{1,*} Yusheng Hou²,² Lei Gu,² and Ruqian Wu^{2,†}

¹State Key Laboratory of Surface Physics and Key Laboratory for Computational Physical Sciences (MOE) and Department of Physics, Fudan University, Shanghai 200433, China

²Department of Physics and Astronomy, University of California, Irvine, California 92697-4575, USA



(Received 7 February 2020; revised manuscript received 1 May 2020; accepted 4 May 2020; published 22 May 2020)

Using the first-principles calculations, we systematically investigated magnetic properties of a MnBi_2Te_4 (MBT) monolayer in contact with $\text{III}_2\text{-VI}_3$ two-dimensional ferroelectric substrates. As the electric polarization in the ferroelectric films is switched, a semiconductor to half-metal transition occurs in MBT, and its magnetic easy axis in several cases reorients. As an example, the Curie temperature of MBT/ In_2Se_3 can be enhanced to 21.5 or 32 K under the influence of electric polarization and biaxial strain, much higher than that of the pristine MBT monolayer, which is 14.5 K in our calculations. Our results suggest effective ways to tune magnetic properties of MBT and provide useful insights for the further development of these important van der Waals functional materials.

DOI: [10.1103/PhysRevB.101.184426](https://doi.org/10.1103/PhysRevB.101.184426)

I. INTRODUCTION

van der Waals (vdW)-type two-dimensional (2D) materials have attracted tremendous research interest as they have high flexibility, excellent integrability, and peculiar quantum properties. Over the past decades, diverse 2D materials have been proposed and synthesized and most of them are promising for the next generation electronic and spintronic applications. Physical properties of typical thin films strongly alter as the thickness is reduced to the monolayer limit. Some common features of their bulk counterparts, such as the long-range ferromagnetic (FM) order and ferroelectric (FE) polarization, may disappear in 2D materials. For example, the long-range magnetic order is precluded in 2D systems at finite temperature according to the Mermin-Wagner theorem [1] based on the isotropic Heisenberg model. Ferromagnetism recently observed in ultrathin CrI_3 [2], CrGeTe_3 [3], Fe_3GeTe_2 [4], VSe_2 [5], and MnSe_x [6] was attributed to the role of out-of-plane magnetic anisotropies that frustrate the thermal fluctuation.

One of the important recent findings in this realm is that the antiferromagnetic (AFM) vdW layered material MnBi_2Te_4 (MBT) is an intrinsic 2D magnetic topological insulator [7,8]. Depending on the thickness, MBT films may exhibit alternating FM or AFM interlayer orders, and manifest different topological phenomena, such as the quantum anomalous Hall effect, Weyl semimetal states, and axion insulator states. The presence of multiple magnetic and topological properties in a single system has inspired extensive studies on MBT, both theoretically [9–15] and experimentally [16–29].

Nevertheless, it remains a challenge to find ways for enhancing the Curie temperature (T_C) of MBT, and for tuning its quantum properties in a large range with energy-efficient approaches.

It has been recognized that vdW 2D films have a weak electric screening effect and hence their physical properties can be effectively tuned by an external electric field which is usually generated by applying a vertical bias or through contacting with a ferroelectric substrate. In particular, the switch of electric polarization in the FE layer, $P \uparrow \rightarrow P \downarrow$ or vice versa, changes the direction of electric field in the adjacent vdW layer and hence alters its quantum properties. To enhance the integrability and diversity of heterostructures, it is desired to develop highly flexible ultrathin FE materials. However, ferroelectricity is rather unusual for 2D materials down to a few monolayers (MLs) in thickness, as the depolarizing electrostatic field and uncompensated surface charge frustrate spontaneous electric polarizations [30–34]. Despite numerous theoretical predictions [35–41], only a few ferroelectric 2D materials have been found experimentally, including CuInP_2S_6 [42] with an out-of-plane electric polarization, and SnTe [43] with an in-plane electric polarization. Interestingly, Ding *et al.* recently predicted a series of vdW 2D ferroelectric materials, such as In_2Se_3 and other $\text{III}_2\text{-VI}_3$ layered materials [41]. Through the first-principles calculations, they found that In_2Se_3 ML may sustain the ferroelectricity up to room temperature with a reversible spontaneous electric polarization. It is exciting that ultrathin In_2Se_3 layers have been successfully synthesized in experiments, with robust ferroelectricity being demonstrated [44–48]. Therefore, $\text{III}_2\text{-VI}_3$ layered materials are ready to be used for the integration with other 2D vdW materials. The lack of surface dangling bonds in both functional and FE layers allows them to be stacked in different

*These authors contributed equally to this work.

†wur@uci.edu

combinations of material types, sequences, and twisting angles, providing immense possibilities to attain high tunability and structure-property coupling in the FE 2D heterostructures. For instance, various fascinating phenomena may emerge in vdW FM/FE heterostructures, including magnetic easy axis change in CrGeTe₃/In₂Se₃ [49], FM to AFM transition in FeI₂/In₂Se₃ [50], and semiconductor to half-metal transition in CrI₃/Sc₂CO₂ [51].

In this work, we performed systematic first-principles calculations for a variety of MBT/FE vdW heterostructures, with different FE layers chosen from III₂-VI₃ combinations (III = Al, Ga, In and VI = Se, Te). The MBT ML is a ferromagnet with an out-of-plane easy axis and a Curie temperature of 14.5 K. The Curie temperature of MBT can be increased to 21.5 K in the MBT/In₂Se₃ heterostructure, due to the field-induced enhancement of both exchange interaction and magnetic anisotropy. Some of these systems show a reorientation of magnetic easy axis in responding to the switch of electric polarization. Furthermore, we found that a semiconductor to half-metal transition may occur when the electric polarization changes direction, a phenomenon which is suitable for use as nano switches. We also found that compressive external biaxial strains may further enhance the T_C of the MBT/In₂Se₃ heterostructure, e.g., to 32 K with a -5% strain. These findings pave the way for the development of MBT/FE films in spintronic and quantum devices.

II. METHODS

The density functional theory (DFT) calculations were performed using the projector augmented wave (PAW) [52,53] method as implemented in the Vienna *ab initio* simulation package (VASP) [54,55]. The exchange-correlation effect among electrons was described within the framework of generalized-gradient approximation (GGA), using the functional proposed by Perdew, Burke, and Ernzerhof (PBE) [56]. For the plane-wave basis expansion, we used an energy cutoff of 350 eV. We utilized a Γ centered $13 \times 13 \times 1$ Monkhorst-Pack \mathbf{k} -point mesh for calculating properties of MBT and MBT/FE heterostructures, and a denser $26 \times 26 \times 1$ mesh for calculating their magnetic anisotropy energies. The convergence with respect to \mathbf{k} -point sampling was carefully tested. The vacuum space between adjacent slabs was set to be 15 Å, which is enough to eliminate the spurious interactions. The in-plane lattice constants and atomic coordinates were fully relaxed using the conjugate gradient method with a criterion that requires the magnitude of force acting on each atom to be smaller than 0.01 eV/Å. The strong electron correlation effect for the localized d orbitals of Mn was treated by an effective on-site Hubbard term [57] of $U = 4$ eV. The vdW corrections were invoked in all calculations, using the DFT-D3 method [58,59].

III. RESULTS

A. Structure and magnetic properties of MBT ML

The bulk MBT crystallizes in a rhombohedral layered structure with the space group $R\bar{3}m$, and each MBT ML consists

of a Te-Bi-Te-Mn-Te-Bi-Te septuple layers (SLs) as shown in Fig. 1(a), where Mn atoms are arranged in a triangular lattice in the central plane. The SLs stack along the perpendicular direction with an ABC sequence. The magnetic moments of Mn atoms in the same SL are parallel to each other and form an in-plane FM order, while the magnetizations of neighboring SLs are opposite in direction, forming an interlayer AFM order [8,13–15,60].

Here, we focus on properties of a free-standing MBT SL. The unit cell used in our calculations is shown by the red dashed quadrilateral in Fig. 1(a), which contains one Mn atom, two Bi atoms, and four Te atoms. The optimized in-plane lattice constants with and without vdW corrections are 4.30 and 4.36 Å, respectively, consistent with previous work [11]. Considering that vdW corrections play a critical role in determining the interlayer space of MBT/FE heterostructures, we adopted the lattice constant of 4.30 Å in all calculations. The calculated magnetic moment is $5\mu_B$ per unit cell, indicating that the Mn atom adopts a high spin configuration ($S = 5/2$) in the ground state. In Fig. 1(b), we present the band structure of the MBT SL with the inclusion of spin orbit coupling (SOC). It can be clearly seen that the MBT SL is a semiconductor with a narrow band gap of 0.28 eV. The valence-band maximum (VBM) is mainly contributed by Te atoms, while the conduction-band minimum (CBM) is dominated by Bi orbitals. The Mn 3d orbitals are far away from the Fermi level, with the majority spin states and minority spin states being fully occupied or empty, respectively.

The magnetic anisotropy energy (MAE) of the MBT SL contains two parts: the shape anisotropy energy (SAE) resulting from magnetic dipole-dipole interactions and the SOC driven magnetocrystalline anisotropy (MCA) energy. In ultrathin films, these two parts are typically comparable [61]. Using the local magnetic moment of Mn and the lattice constant, we found that SAE of the MBT SL is -0.14 meV per unit cell, where the negative sign means that the SAE term leads to the in-plane magnetization. The MCA term is calculated using the torque method proposed by Wang *et al.* [62,63]:

$$\text{MCA} = E_x^{\text{SOC}} - E_z^{\text{SOC}} = \sum_{\mathbf{k}} \sum_{i \in \text{occ}} \langle \psi_{i,\mathbf{k}} | \frac{\partial H_{\text{SOC}}}{\partial \theta} | \psi_{i,\mathbf{k}} \rangle_{\theta=45^\circ}, \quad (1)$$

where $|\psi_{i,\mathbf{k}}\rangle$ is the wave function of the i th state at the \mathbf{k} point, H_{SOC} is the SOC Hamiltonian, and θ is the polar angle of spin. The summation runs over all occupied states and all \mathbf{k} points in the entire Brillouin zone. The calculated MCA value is 0.18 meV per unit cell, in good agreement with previous report (0.18 meV) [11]. We also used the direct total energy approach as $\text{MCA} = E_x^{\text{SOC}} - E_z^{\text{SOC}} = 0.17$ meV, indicating that both torque and total-energy approaches work well for the present system. As a result, the total MAE is only 0.04 meV/Mn, with an out-of-plane easy axis.

The torque method allows us to further decompose the MCA into contributions from different atoms by writing

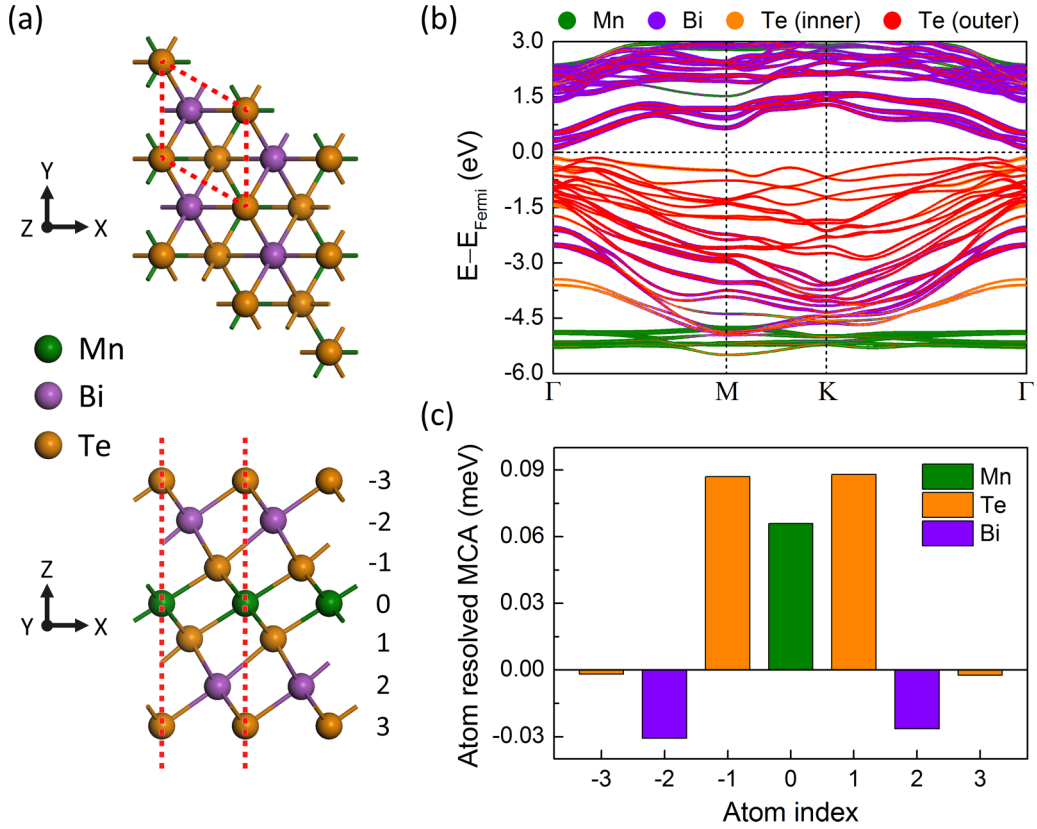


FIG. 1. (a) Top and side views of the MBT ML. The unit cell is indicated by the red dashed quadrilateral. Olive, violet, and orange balls represent Mn, Bi, and Te atoms, respectively. (b) Band structure of the MBT ML with SOC. States of Mn, Bi, inner Te, and outer Te atoms are represented by olive, violet, orange, and red lines, respectively, and the linewidth scales with their weights. (c) Atom resolved MCA of the MBT ML. The corresponding atom indices are labeled in (a), and the colors of the bars represent different atoms.

Eq. (1) as

$$\begin{aligned}
 \text{MCA} &= \sum_{\mathbf{k}} \sum_{i \in \text{occ}} \left(\sum_{\mathbf{G}} \sum_{\alpha} \sum_{l, m, s} c_{i, \mathbf{k} + \mathbf{G}}^{* \alpha, l, m, s} \langle \chi_{\alpha, l, m, s} | \right) \frac{\partial H_{\text{SOC}}}{\partial \theta} \left(\sum_{\mathbf{G}} \sum_{\alpha} \sum_{l, m, s} c_{i, \mathbf{k} + \mathbf{G}}^{\alpha, l, m, s} | \chi_{\alpha, l, m, s} \rangle \right) \Big|_{\theta=45^\circ} \\
 &= \sum_{\alpha} \sum_{\mathbf{k}} \sum_{i \in \text{occ}} \sum_l \sum_{m, m', s, s'} \sum_{\mathbf{G}, \mathbf{G}'} c_{i, \mathbf{k} + \mathbf{G}}^{* \alpha, l, m, s} c_{i, \mathbf{k} + \mathbf{G}'}^{\alpha, l, m', s'} \langle \chi_{\alpha, l, m, s} | \frac{\partial H_{\text{SOC}}}{\partial \theta} | \chi_{\alpha, l, m', s'} \rangle \Big|_{\theta=45^\circ} = \sum_{\alpha} \text{MCA}_{\alpha}, \quad (2)
 \end{aligned}$$

where α denotes the atom index, \mathbf{G} are all reciprocal-lattice vectors up to $|\mathbf{k} + \mathbf{G}| \leq \mathbf{k}_{\text{max}}$, l , m , and s are angular momentum, magnetic, and spin quantum numbers, respectively. c is the projection coefficient of wave function on the basis function χ . Here, we used the fact that H_{SOC} is a local operator and does not change the value of l , so only matrix elements with the same α and l are nonzero. The MCA contribution from the α th atom is then represented by MCA_{α} , which can be understood by the torque moments exerted on that atom, even though these moments are not independent since in torque formula all the moments are assumed to rotate at the same time. Figure 1(c) shows the atom resolved MCA contributions that are determined by Eq. (2) in the MBT SL. It is found that Mn atom contributes $\sim 1/3$ of the MCA, and its adjacent two Te atoms contribute $\sim 2/3$. This is different from CrI_3 and CrGeTe_3 , for which the magnetic atoms have negligible contributions to MCA.

To determine the exchange parameters J_i between Mn atoms, we expanded the unit cell and mapped the DFT total energies of four different magnetic configurations (Fig. S1 in the Supplemental Material [64]) onto the following classical Heisenberg Hamiltonian:

$$\begin{aligned}
 H &= -J_1 \sum_{\langle ij \rangle} \vec{S}_i \cdot \vec{S}_j - J_2 \sum_{\langle\langle ij \rangle\rangle} \vec{S}_i \cdot \vec{S}_j \\
 &\quad - J_3 \sum_{\langle\langle\langle ij \rangle\rangle\rangle} \vec{S}_i \cdot \vec{S}_j, \quad (3)
 \end{aligned}$$

where J_1 , J_2 , and J_3 represent the nearest-, next-nearest-, and third-nearest-neighbor exchange interactions, respectively. Obviously, positive values of J_i ($i = 1, 2$, and 3) mean FM interaction, while negative ones mean AFM interaction. Based on Eq. (3), the total energies of the four spin configurations shown in Fig. S1 are given as

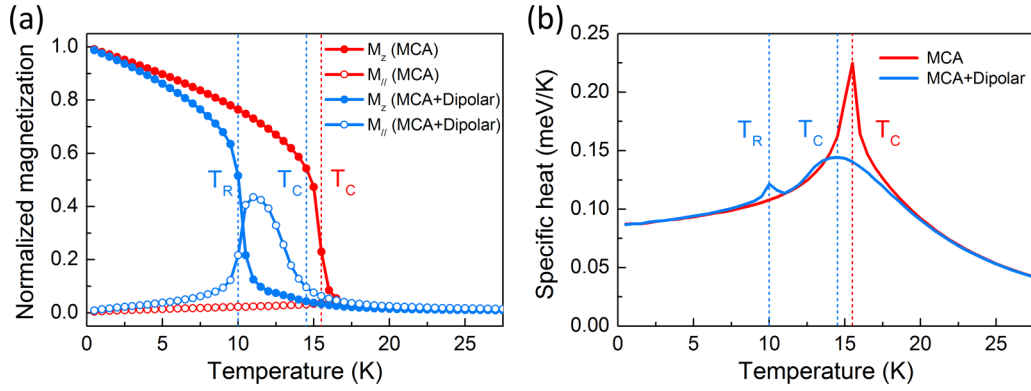


FIG. 2. MC simulations of MBT ML. (a) The renormalized magnetization $M(T)/M_0$ of the MBT ML as a function of temperature T . The blue and red lines represent results with and without dipole-dipole interactions, respectively. Solid symbols indicate out-of-plane magnetization, while unfilled symbols denote in-plane magnetization. (b) Specific heat of the MBT ML. The T_R and T_C are extracted from the maximum of specific heat.

follows:

$$\begin{aligned}
 E_{\text{FM}} &= E_0 - 24J_1|\bar{S}|^2 - 24J_2|\bar{S}|^2 - 24J_3|\bar{S}|^2, \\
 E_{\text{AFM}}^{\text{stripy}} &= E_0 + 8J_1|\bar{S}|^2 + 8J_2|\bar{S}|^2 - 24J_3|\bar{S}|^2, \\
 E_{\text{AFM}}^{\text{zigzag1/zigzag2}} &= E_0 \mp 8J_1|\bar{S}|^2 \pm 8J_2|\bar{S}|^2 + 8J_3|\bar{S}|^2.
 \end{aligned} \quad (4)$$

From the total energies, we found that $J_1 = 1.26$ meV, $J_2 = -0.12$ meV, and $J_3 = 0.03$ meV for the MBT SL, close to what were found in previous studies [11]. The nearest-neighbor exchange interaction (J_1) is dominating for the establishment of the FM ground state. The next-nearest-neighbor interaction (J_2) prefers the AFM ordering, and the third-nearest-neighbor interaction (J_3) is FM again.

We then determined the T_C of MBT SL by performing Monte Carlo (MC) simulations based on a classical 2D Heisenberg model, with both the on-site MCA and long-range dipole-dipole interactions included. The model is described by the following Hamiltonian:

$$\begin{aligned}
 H = & -\frac{1}{2} \sum_{i,j} J_{ij} \bar{S}_i \cdot \bar{S}_j - K \sum_i (S_i^z)^2 \\
 & + \frac{1}{2} \frac{\mu_0 g^2 \mu_B^2}{4\pi} \sum_{i,j} \left[\frac{\bar{S}_i \cdot \bar{S}_j}{|\bar{r}_{ij}|^3} - 3 \frac{(\bar{S}_i \cdot \bar{r}_{ij})(\bar{S}_j \cdot \bar{r}_{ij})}{|\bar{r}_{ij}|^5} \right], \quad (5)
 \end{aligned}$$

where the first term denotes the short-range exchange interactions up to third nearest neighbors, the second term is the on-site MCA energy which is 0.18 meV/Mn from our calculations, and the last term refers to the long-range dipole-dipole interactions which introduce an in-plane SAE of -0.14 meV/Mn. Here, μ_0 is the vacuum permeability, g is the electron spin g factor, μ_B is the Bohr magneton, and r_{ij} is the vector connecting site i and j . Our MC simulations were carried out on a 100×100 lattice with periodic boundary conditions. The summation of the long-range dipolar interactions runs over the whole lattice as well as all the periodic images in the range of $r_{ij} < 10^4$ a.u. We used 10^5 MC steps per site to equilibrate the system, and 10^7 MC steps per site for statistical averaging.

The simulated magnetization as a function of temperature is shown in Fig. 2(a), in which the red and blue lines represent results with and without dipolar interactions, respectively. In the absence of dipolar interactions, the out-of-plane magnetization drops rapidly to zero at T_C , while the in-plane magnetization remains zero over the whole temperature range. When the dipolar interactions are considered, an intriguing temperature driven reorientation transition of the magnetization was observed. At low temperature, the system exhibits an out-of-plane FM phase. With increasing the temperature to a critical value of T_R , the out-of-plane magnetization suddenly vanishes, accompanied by a sharp rise of in-plane magnetization. As the temperature increases further, the in-plane magnetization decreases and eventually reaches a paramagnetic phase above T_C .

Such a temperature driven reorientation transition near T_R can be understood by the competition between the perpendicular MCA and the in-plane SAE that resulted from long-range dipolar interactions. It is worth mentioning that, for FM films, although the dipolar interactions favor an in-plane SAE, it differs significantly from an effective on-site in-plane MCA, since the former does break the conditions of the Mermin-Wagner theorem, and can sustain long-range magnetic order in 2D systems [65]. In fact, a similar reorientation transition has also been observed experimentally in Fe/Cu(001) films [66], and has been studied rather extensively in theory [67–73].

The accurate values of T_R and T_C can be extracted from the maximum of specific heat as shown in Fig. 2(b). In the absence of dipolar interactions, the specific heat shows one sharp peak, indicating a T_C of 15.5 K. When the dipolar interactions are considered, it exhibits two distinct peaks. The former corresponds to the out-of-plane to in-plane transition temperature $T_R = 10$ K, while the latter is the Curie temperature $T_C = 14.5$ K. Such a value is in excellent agreement with a previous theoretical study of 12 K, although they adopted a different value of Hubbard U , more numbers of neighbors, and simply treated dipolar interactions as an effective in-plane MCA [13]. Our calculated T_C also matches well with experimental measurements for weakly coupled MBT SLs in (MBT)(Bi₂Te₃)_m heterostructures (10–12 K) [7,28,29].

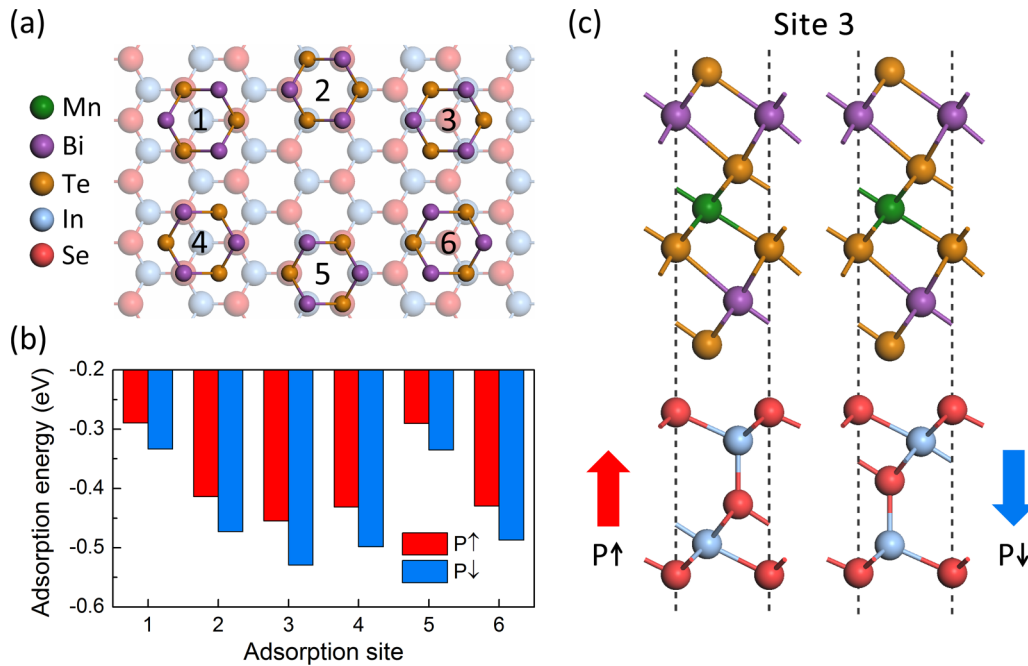


FIG. 3. (a) The six possible alignments of MBT/In₂Se₃ heterostructures. Only the interfacial atoms from each side of the interface are shown here. Sites 1, 2, and 3 are for the outmost Te atoms in MBT sitting at the top Se, top-In, and hollow sites of In₂Se₃, respectively, and sites 4, 5, 6 are obtained by applying a 60° rotation from 1, 2, 3. (b) The adsorption energies of each configuration in (a). (c) The side views of the most stable geometry with the electric dipole of In₂Se₃ pointing upward and downward ($P \uparrow$ and $P \downarrow$), respectively.

B. Semiconductor to half-metal transition and reorientation of magnetic easy axis in MBT/FE heterostructures

We now investigate how to control the physical properties of MBT ML using FE layers such as In₂Se₃. The In₂Se₃ ML has two energetically degenerate ferroelectric ground states in either the zinc-blende or the Wurtzite structure [41]. In this study, we mainly focused on the zinc-blende one and construct the MBT/In₂Se₃ heterostructure as shown in Fig. 3. The optimized lattice constant of the In₂Se₃ ML with vdW corrections is 4.10 Å, about 6.0% smaller than that of MBT ML (4.30 Å). For the simplicity of calculations and discussions, we stretched the lattice of the In₂Se₃ ML to match that of MBT ML. This is reasonable as the polarization of In₂Se₃ changes very little under a biaxial strain [41]. We considered six possible alignments between MBT and In₂Se₃ as shown in Fig. 3(a), with the outmost Te atoms in MBT sitting at the top-Se, top-In, and hollow sites of In₂Se₃ and three other sites. Their corresponding adsorption energies are given in Fig. 3(b) for both the up and down electric polarizations. Clearly, the most stable structure is configuration 3 in Fig. 3(a) for both $P \uparrow$ and $P \downarrow$, i.e., with Te atoms sitting over the hollow sites of In₂Se₃ as illustrated in Fig. 3(c).

As shown in Fig. S2 of the Supplemental Material [64], the freestanding MBT and In₂Se₃ MLs are both semiconductors, with band gaps of 0.28 and 0.44 eV in our calculations, respectively. When they are stacked in a heterostructure, an electric field is built across the interface and penetrates into MBT as well. This should dramatically modify the electronic properties of MBT and offers a handle to control them. In Fig. 4, we display the band structures of MBT/In₂Se₃ with both up and down polarizations. The system retains the semiconductor nature for the up polarization, and the band gap

is slightly reduced to 0.25 eV. Interestingly, the Fermi level crosses majority spin bands [red lines in Fig. 4(d)] of MBT for the down polarization, leading to a half-metal behavior in MBT and some conduction in In₂Se₃ as well. Hence, by controlling the two FE In₂Se₃ states with opposite electric polarization directions, the MBT/In₂Se₃ heterostructure can be switched between semiconductor and half metal. Note that such a switching behavior is robust, unchanged by using different Hubbard U values or the HSE06 hybrid functional in calculations [74] (Fig. S3 of the Supplemental Material [64]). This phenomenon may therefore find important applications such as nano switches and rectification junctions in spintronic devices.

To understand the mechanism of such a polarization driven semiconductor/half-metal transition, we calculated the band alignments of MBT/In₂Se₃ by using the method sketched in Fig. S4 [64]. In Fig. 5(b), the VBM and CBM are obtained from free-standing MBT and In₂Se₃, therefore the CBM of In₂Se₃ in MBT/In₂Se₃(\uparrow) in Fig. 4(a) looks slightly higher than that in Fig. 5(b) due to band hybridizations in the heterostructure. Because of the inherent electric field, there is a potential drop of 1.078 eV across the two sides of In₂Se₃ [Fig. 5(a)], leading to distinctly different band shifts in MBT when contacting with opposite sides. When the polarization is upward, the CBM of In₂Se₃ locates above the VBM of MBT. Therefore, the electrons cannot transfer between MBT and In₂Se₃, but are slightly redistributed in the interfacial region. In contrast, for the downward polarization, the CBM of In₂Se₃ becomes lower than the VBM of MBT, leading to electron transfers from MBT to In₂Se₃. This can also be seen from the projected density of states (PDOS) in Fig. 5(c), in which the relative shifts are depicted between MBT and In₂Se₃ bands. As the polarization is switched to the downward direction, the

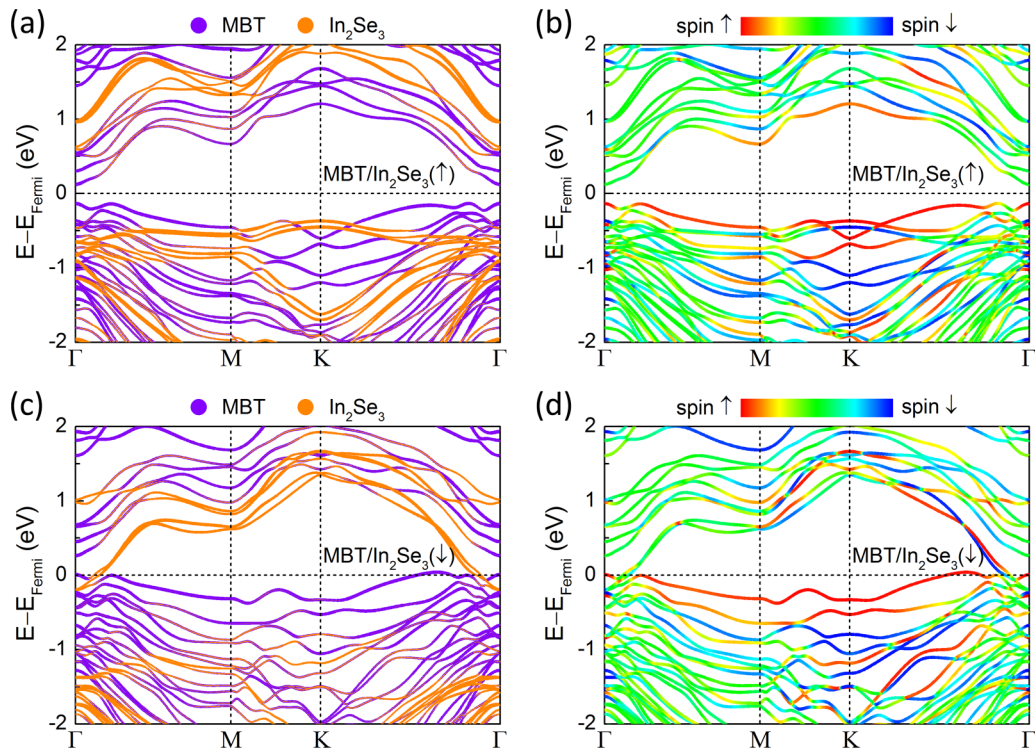


FIG. 4. Band structures of MBT/ In_2Se_3 with SOC. Panels (a) and (b) are decomposed on each component and on each spin channel for up polarization, and (c) and (d) are for down polarization.

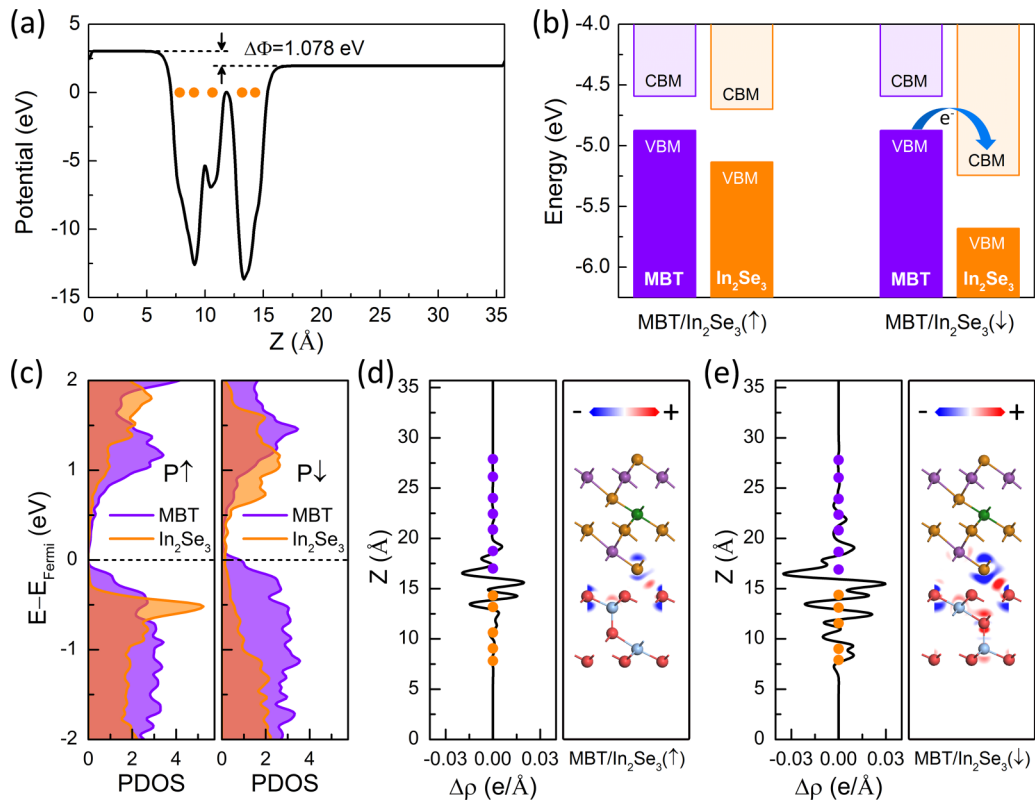


FIG. 5. (a) The planar-averaged electrostatic potential of the In_2Se_3 ML. The orange dots represent positions of atoms. (b) Band alignments of $\text{MBT/In}_2\text{Se}_3(\uparrow)$ and $\text{MBT/In}_2\text{Se}_3(\downarrow)$ with respect to the vacuum level of MBT. (c) PDOS of $\text{MBT/In}_2\text{Se}_3(\uparrow)$ and $\text{MBT/In}_2\text{Se}_3(\downarrow)$. (d), (e) Planar averaged and 2D charge density difference of $\text{MBT/In}_2\text{Se}_3$ heterostructure. The violet and orange dots represent positions of MBT and In_2Se_3 atoms, respectively. The blue and red areas indicate loss and gain electrons, respectively.

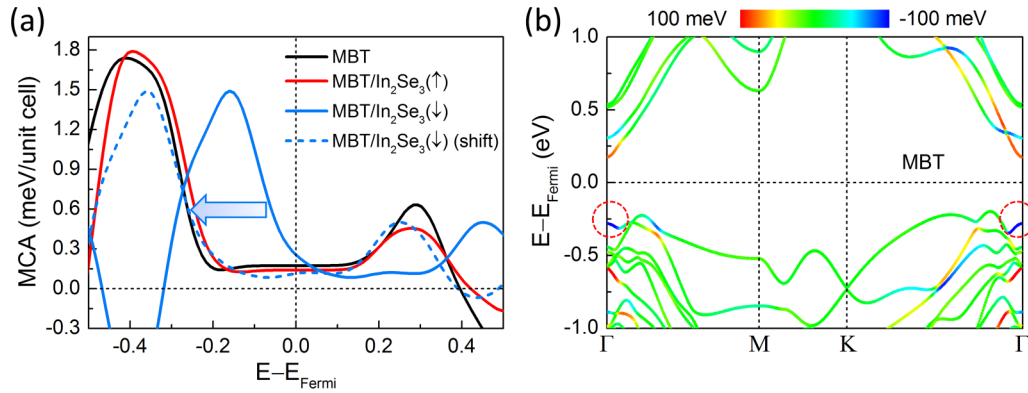


FIG. 6. (a) MCA change as a function of the shift of Fermi energy for MBT ML, MBT/In₂Se₃(↑), and MBT/In₂Se₃(↓). The blue dashed line is shifted by -0.2 eV from the blue solid line. (b) Band resolved MCA for the MBT ML. The red and blue colors represent positive and negative contributions, respectively. Here the band structure is calculated with the magnetization at $\theta = 45^\circ$.

CBM of In₂Se₃ overlaps with the VBM of MBT. Furthermore, the planar averaged plots of charge transfer are shown in Figs. 5(d) and 5(e). Clearly, the charge transfer is restricted in the interface region for the upward polarization but spreads over all In₂Se₃ layers for the downward polarization.

The distinct change of electronic structures between upward and downward electric polarizations in the MBT/In₂Se₃ heterostructure should also affect its magnetic properties, such as the exchange interactions and MCA. Indeed, we find that the downward polarization induces significant enhancements for both J_1 (to 1.84 meV) and MCA (to 0.26 meV), resulting in an increase of T_C to 21.5 K according to the MC simulations with new parameters in Eq. (5). This primarily results from the interfacial charge transfer rather than the small structural change, since both J_1 and MCA restore their values in the isolated MBT MSL after we remove the In₂Se₃ substrate but keep the atomic positions of MBT intact as in the heterostructure.

To further understand the modification of MCA, we present in Fig. 6(a) the MCA changes as the Fermi energy (E_F) is shifted in a range of ± 0.5 eV for the pristine MBT ML, MBT/In₂Se₃(↑) and MBT/In₂Se₃(↓). Clearly, profiles of their MCA(E_F) curves are almost the same, except that for MBT/In₂Se₃(↓) for which the curve has an upward shift of about 0.2 eV. The MCA of the MBT ML can be

significantly enhanced by either adding or removing electrons according to this rigid-band analysis. As the charge transfer in MBT/In₂Se₃(↑) is negligible, its MCA is not much changed from that of the pristine MBT ML. Obviously, the inversion of electric field and charge transfer in MBT/In₂Se₃(↓) play the key role for the enhancement of its MCA. The torque method allows us to further decompose the MCA of MBT ML to each band as shown in Fig. 6(b). Here, the colors of bands indicate their torques as the magnetization is set at $\theta = 45^\circ$ according to Eq. (1) [the band structures are slightly different from those in Fig. 1(b) because of the change of SOC contributions]. Clearly, the first band at -0.28 eV near the Γ point has a large negative contribution to the MCA, as highlighted by the red dashed circle. When the MBT ML loses electrons, this band shifts to above the Fermi level and the removal of its negative contribution results in an increase of positive MCA.

We further extended our studies to other III₂-VI₃ FE substrates, including Al₂Te₃, Ga₂Te₃, and In₂Te₃ (their lattice mismatches with MBT are -5.5% , -4.9% , and 0.5% , respectively). The band structures of these heterostructures are shown in Fig. S5 of the Supplemental Material [64]. MBT with Al₂Te₃, Ga₂Te₃ remains to be a semiconductor as we switch the polarization in the FE layer. In contrast, MBT/In₂Te₃(↑) shows even stronger response to the

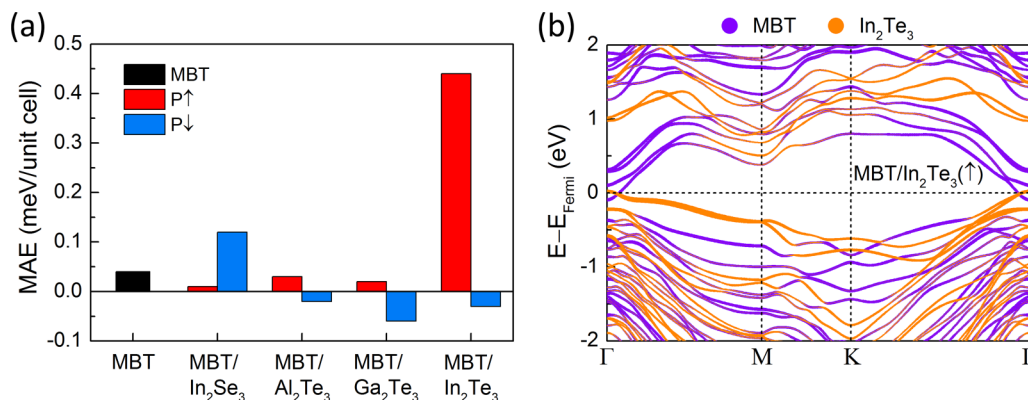


FIG. 7. (a) The calculated MAE of MBT/FE heterostructures with up and down polarizations. (b) Band structure of MBT/In₂Te₃(↑) with SOC.

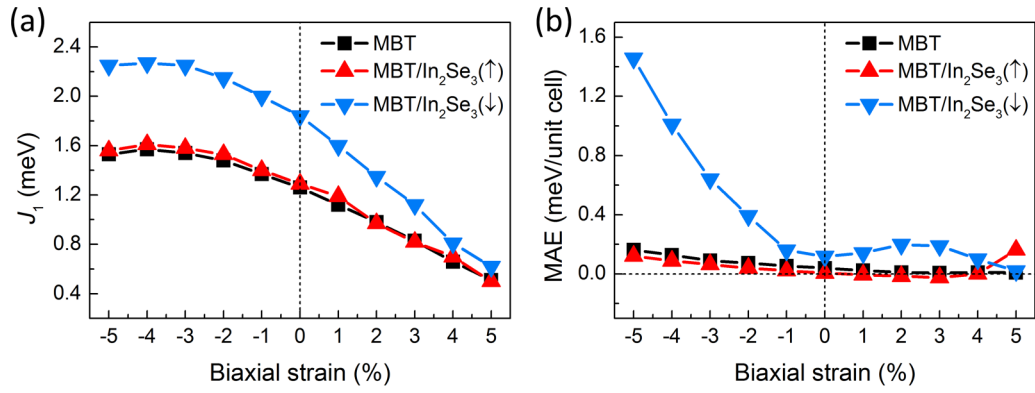


FIG. 8. (a) The exchange interaction J_1 and (b) MAE as a function of the biaxial strain. Black, red, and blue lines represent MBT, MBT/In₂Se₃(↑), and MBT/In₂Se₃(↓), respectively.

change of polarization than MBT/In₂Se₃ does. Not only the semiconductor/half-metal transition occurs, the MAE can also be effectively tuned as shown in Fig. 7(a). Note that SAEs are already included in the MAE values in Fig. 7(a). It can be clearly seen that the easy axis can be changed by switching the electric polarization direction for most three heterostructures. As the magnetic moment of Mn remains the same in all these systems, the SAE does not change. In contrast, MCA is sensitive to the interfacial hybridization and charge redistribution. Specifically, the MBT/In₂Te₃(↑) possesses a total MAE as large as 0.44 meV/Mn due to the charge transfer from In₂Te₃ to MBT, as evidenced by the band structure shown in Fig. 7(b). As shown in Fig. 6(b), the first band at the Γ point above the Fermi level has a positive MCA. It shifts down to below Fermi energy in MBT/In₂Te₃(↑) and hence gives rise to an increase of positive MAE. As the lattice mismatch is also the smallest among these heterostructures, MBT/In₂Te₃ appears to be a practical candidate for realizing efficient electric control of magnetic and transport properties of 2D MBT/FE heterostructures.

It is known the MBT families exhibit many interesting topological properties. A natural question to ask is whether the MBT ML may become topologically nontrivial as it in contact with FE substrates. We therefore calculated the Chern number of the MBT ML and all semiconducting MBT/FE heterostructure. The results are summarized in

Fig. S6 of the Supplemental Material [64]. Clearly, none of these systems are topologically nontrivial. This is understandable because that the FE substrates don't hybridize strongly with the MBT to cause band inversions as shown in Fig. S5 [64].

C. Effects of external biaxial strains on MBT/FE heterostructures

Lattice strain is another effective means for the manipulation of magnetic properties of MBT or MBT/FE heterostructures. In Figs. 8(a) and 8(b), we plot J_1 and MAE of the free-standing MBT ML and MBT/In₂Se₃ (for both upward and downward polarizations) as a function of biaxial strains. When we apply a compressive strain, the exchange parameter J_1 of the MBT ML increases monotonically and reaches its maximum at about -4% strain. Such a behavior originates from the fact that the Te-Mn-Te bond angle gradually approaches 90° as reported by Li *et al.* [11]. The MAE of the MBT ML also slowly enhances with the compressive strain. The presence of the In₂Se₃ substrate with an upward electric polarization has negligible effect on both J_1 and MAE in the entire strain range. However, when the In₂Se₃ substrate has a downward electric polarization the compressive strain may significantly enhance J_1 and MAE, to 2.25 and 1.48 meV at -5% , respectively. As a result, the T_C is increased to 32 K,

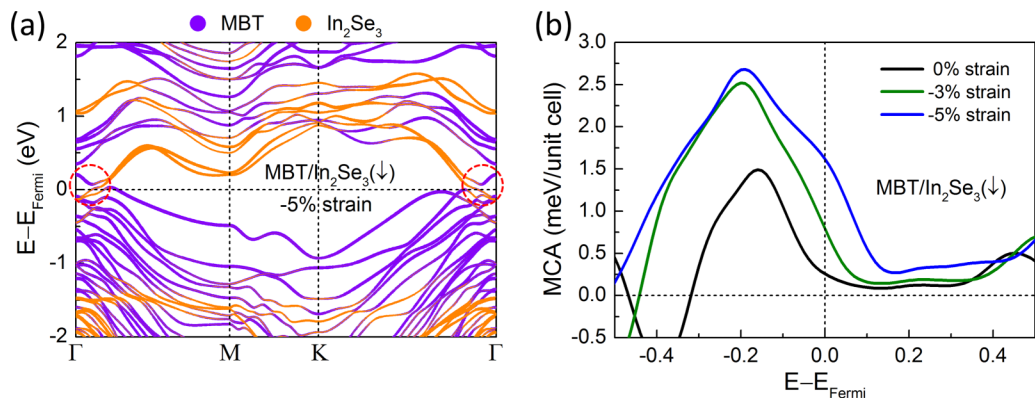


FIG. 9. (a) Band structure of MBT/In₂Se₃(↓) under -5% strain calculated with SOC. The violet and orange lines represent components of MBT and In₂Se₃, respectively. (b) MCA of MBT/In₂Se₃(↓) as a function of the shift of Fermi energy with strains 0%, -3% , and -5% .

which is twice as large as the value of the free-standing MBT ML without strains.

Such a giant enhancement of MAE for MBT/ $\text{In}_2\text{Se}_3(\downarrow)$ under compressive strains can be understood in terms of charge transfers. In Fig. 9(a), we plot the band structure of MBT/ $\text{In}_2\text{Se}_3(\downarrow)$ under a -5% strain. Compared to the one without strain [Fig. 4(c)], the Fermi level is pushed down to a much lower position below the VBM of MBT as highlighted by the red dashed circles in Fig. 9(a), indicating that additional electron transfer from MBT to In_2Se_3 is produced by the compressive strain. According to the rigid-band model analysis depicted in Fig. 6(a), the MCA of MBT increases as it loses electrons. To give more direct evidence, we show curves of MCA versus the position of the Fermi energy for MBT/ $\text{In}_2\text{Se}_3(\downarrow)$ under 0% , -3% and -5% strains in Fig. 9(b). It shows that the compressive strains gradually shift the curve to the right side, resulting in a steady increase of MCA.

IV. SUMMARY

In summary, we systematically investigated the possibility of tuning magnetic properties of the MBT ML by using the

proximity effect with 2D FE $\text{III}_2\text{-VI}_3$ ($\text{III} = \text{Al, Ga, In, and VI} = \text{Se, Te}$) substrates and by applying biaxial strains as well. For the MBT/ In_2Se_3 heterostructure, a transition between semiconductor and half metal can be induced when the electric polarization is switched from up to down, accompanied by an enhanced exchange interactions and MCA. As a result, the T_C can be raised from 14.5 K for the pristine MBT ML to 21.5 K for MBT/ In_2Se_3 . The enhancement of MCA is attributed to the charge transfers induced by the interfacial electric field. We further predicted a polarization induced change of the magnetic easy axis in MBT as it is placed on the Al_2Te_3 , Ga_2Te_3 , and In_2Te_3 substrates. Furthermore, T_C of MBT/ $\text{In}_2\text{Se}_3(\downarrow)$ can be further enhanced to 32 K by applying a -5% strain. These results provide an effective way to realize nonvolatile control of spintronic devices based on 2D vdW heterostructures.

ACKNOWLEDGMENTS

This work was supported by the US Department of Energy, Office of Science, Basic Energy Sciences under Award No. DE-FG02-05ER46237 and the National Energy Research Scientific Computing Center (NERSC).

-
- [1] N. D. Mermin and H. Wagner, *Phys. Rev. Lett.* **17**, 1133 (1966).
 [2] B. Huang, G. Clark, E. Navarro-Moratalla, D. R. Klein, R. Cheng, K. L. Seyler, D. Zhong, E. Schmidgall, M. A. McGuire, D. H. Cobden, W. Yao, D. Xiao, P. Jarillo-Herrero, and X. Xu, *Nature (London)* **546**, 270 (2017).
 [3] C. Gong, L. Li, Z. Li, H. Ji, A. Stern, Y. Xia, T. Cao, W. Bao, C. Wang, Y. Wang, Z. Q. Qiu, R. J. Cava, S. G. Louie, J. Xia, and X. Zhang, *Nature (London)* **546**, 265 (2017).
 [4] Z. Fei, B. Huang, P. Malinowski, W. Wang, T. Song, J. Sanchez, W. Yao, D. Xiao, X. Zhu, A. F. May, W. Wu, D. H. Cobden, J.-H. Chu, and X. Xu, *Nat. Mater.* **17**, 778 (2018).
 [5] M. Bonilla, S. Kolekar, Y. Ma, H. C. Diaz, V. Kalappattil, R. Das, T. Eggers, H. R. Gutierrez, M.-H. Phan, and M. Batzill, *Nat. Nanotechnol.* **13**, 289 (2018).
 [6] D. J. O'Hara, T. Zhu, A. H. Trout, A. S. Ahmed, Y. K. Luo, C. H. Lee, M. R. Brenner, S. Rajan, J. A. Gupta, D. W. McComb, and R. K. Kawakami, *Nano Lett.* **18**, 3125 (2018).
 [7] E. D. L. Rienks, S. Wimmer, J. Sánchez-Barriga, O. Caha, P. S. Mandal, J. Růžička, A. Ney, H. Steiner, V. V. Volobuev, H. Groiss, M. Albu, G. Kothleitner, J. Michalička, S. A. Khan, J. Minár, H. Ebert, G. Bauer, F. Freyse, A. Varykhalov, O. Rader *et al.*, *Nature (London)* **576**, 423 (2019).
 [8] M. M. Otrokov, I. I. Klimovskikh, H. Bentmann, D. Estyunin, A. Zeugner, Z. S. Aliev, S. Gaß, A. U. B. Wolter, A. V. Koroleva, A. M. Shikin, M. Blanco-Rey, M. Hoffmann, I. P. Rusinov, A. Y. Vyazovskaya, S. V. Eremeev, Y. M. Koroteev, V. M. Kuznetsov, F. Freyse, J. Sánchez-Barriga, I. R. Amiraslanov *et al.*, *Nature (London)* **576**, 416 (2019).
 [9] Y. Peng and Y. Xu, *Phys. Rev. B* **99**, 195431 (2019).
 [10] J. Li, C. Wang, Z. Zhang, B.-L. Gu, W. Duan, and Y. Xu, *Phys. Rev. B* **100**, 121103(R) (2019).
 [11] Y. Li, Z. Jiang, J. Li, S. Xu, and W. Duan, *Phys. Rev. B* **100**, 134438 (2019).
 [12] J. Zhang, Z. Liu, and J. Wang, *Phys. Rev. B* **100**, 165117 (2019).
 [13] M. M. Otrokov, I. P. Rusinov, M. Blanco-Rey, M. Hoffmann, A. Y. Vyazovskaya, S. V. Eremeev, A. Ernst, P. M. Echenique, A. Arnau, and E. V. Chulkov, *Phys. Rev. Lett.* **122**, 107202 (2019).
 [14] D. Zhang, M. Shi, T. Zhu, D. Xing, H. Zhang, and J. Wang, *Phys. Rev. Lett.* **122**, 206401 (2019).
 [15] J. Li, Y. Li, S. Du, Z. Wang, B.-L. Gu, S.-C. Zhang, K. He, W. Duan, and Y. Xu, *Sci. Adv.* **5**, eaaw5685 (2019).
 [16] S. Zhang, R. Wang, X. Wang, B. Wei, B. Chen, H. Wang, G. Shi, F. Wang, B. Jia, Y. Ouyang, F. Xie, F. Fei, M. Zhang, X. Wang, D. Wu, X. Wan, F. Song, H. Zhang, and B. Wang, *Nano Lett.* **20**, 709 (2020).
 [17] B. Chen, F. Fei, D. Zhang, B. Zhang, W. Liu, S. Zhang, P. Wang, B. Wei, Y. Zhang, Z. Zuo, J. Guo, Q. Liu, Z. Wang, X. Wu, J. Zong, X. Xie, W. Chen, Z. Sun, S. Wang, Y. Zhang *et al.*, *Nat. Commun.* **10**, 4469 (2019).
 [18] J. Cui, M. Shi, H. Wang, F. Yu, T. Wu, X. Luo, J. Ying, and X. Chen, *Phys. Rev. B* **99**, 155125 (2019).
 [19] J. Q. Yan, S. Okamoto, M. A. McGuire, A. F. May, R. J. McQueeney, and B. C. Sales, *Phys. Rev. B* **100**, 104409 (2019).
 [20] R. C. Vidal, H. Bentmann, T. R. F. Peixoto, A. Zeugner, S. Moser, C. H. Min, S. Schatz, K. Kißner, M. Ünzelmann, C. I. Fornari, H. B. Vasili, M. Valvidares, K. Sakamoto, D. Mondal, J. Fujii, I. Vobornik, S. Jung, C. Cacho, T. K. Kim, R. J. Koch *et al.*, *Phys. Rev. B* **100**, 121104(R) (2019).
 [21] T. Murakami, Y. Nambu, T. Koretsune, G. Xiangyu, T. Yamamoto, C. M. Brown, and H. Kageyama, *Phys. Rev. B* **100**, 195103 (2019).
 [22] J. Q. Yan, Q. Zhang, T. Heitmann, Z. Huang, K. Y. Chen, J. G. Cheng, W. Wu, D. Vaknin, B. C. Sales, and R. J. McQueeney, *Phys. Rev. Mater.* **3**, 064202 (2019).
 [23] K. Y. Chen, B. S. Wang, J. Q. Yan, D. S. Parker, J. S. Zhou, Y. Uwatoko, and J. G. Cheng, *Phys. Rev. Mater.* **3**, 094201 (2019).

- [24] Y.-J. Hao, P. Liu, Y. Feng, X.-M. Ma, E. F. Schwier, M. Arita, S. Kumar, C. Hu, R. e. Lu, M. Zeng, Y. Wang, Z. Hao, H.-Y. Sun, K. Zhang, J. Mei, N. Ni, L. Wu, K. Shimada, C. Chen, Q. Liu, and C. Liu, *Phys. Rev. X* **9**, 041038 (2019).
- [25] H. Li, S.-Y. Gao, S.-F. Duan, Y.-F. Xu, K.-J. Zhu, S.-J. Tian, J.-C. Gao, W.-H. Fan, Z.-C. Rao, J.-R. Huang, J.-J. Li, D.-Y. Yan, Z.-T. Liu, W.-L. Liu, Y.-B. Huang, Y.-L. Li, Y. Liu, G.-B. Zhang, P. Zhang, T. Kondo *et al.*, *Phys. Rev. X* **9**, 041039 (2019).
- [26] Y. J. Chen, L. X. Xu, J. H. Li, Y. W. Li, H. Y. Wang, C. F. Zhang, H. Li, Y. Wu, A. J. Liang, C. Chen, S. W. Jung, C. Cacho, Y. H. Mao, S. Liu, M. X. Wang, Y. F. Guo, Y. Xu, Z. K. Liu, L. X. Yang, and Y. L. Chen, *Phys. Rev. X* **9**, 041040 (2019).
- [27] H. Li, S. Liu, C. Liu, J. Zhang, Y. Xu, R. Yu, Y. Wu, Y. Zhang, and S. Fan, *Phys. Chem. Chem. Phys.* **22**, 556 (2020).
- [28] J. Wu, F. Liu, M. Sasase, K. Ienaga, Y. Obata, R. Yukawa, K. Horiba, H. Kumigashira, S. Okuma, T. Inoshita, and H. Hosono, *Sci. Adv.* **5**, eaax9989 (2019).
- [29] I. I. Klimovskikh, M. M. Otrokov, D. Estyunin, S. V. Ereemeev, S. O. Filnov, A. Koroleva, E. Shevchenko, V. Voroshnin, I. P. Rusinov, M. Blanco-Rey, M. Hoffmann, Z. S. Aliev, M. B. Babanly, I. R. Amiraslanov, N. A. Abdullayev, V. N. Zverev, A. Kimura, O. E. Tereshchenko, K. A. Kokh, L. Petaccia *et al.*, [arXiv:1910.11653](https://arxiv.org/abs/1910.11653).
- [30] J. Junquera and P. Ghosez, *Nature (London)* **422**, 506 (2003).
- [31] N. Sai, A. M. Kolpak, and A. M. Rappe, *Phys. Rev. B* **72**, 020101(R) (2005).
- [32] Y. Umeno, B. Meyer, C. Elsässer, and P. Gumbsch, *Phys. Rev. B* **74**, 060101(R) (2006).
- [33] G. Gerra, A. K. Tagantsev, N. Setter, and K. Parlinski, *Phys. Rev. Lett.* **96**, 107603 (2006).
- [34] J. He, G. B. Stephenson, and S. M. Nakhmanson, *J. Appl. Phys.* **112**, 054112 (2012).
- [35] Z. Guan, H. Hu, X. Shen, P. Xiang, N. Zhong, J. Chu, and C. Duan, *Adv. Electron. Mater.* **6**, 1900818 (2020).
- [36] M. Wu and P. Jena, *WIREs Comput. Mol. Sci.* **8**, e1365 (2018).
- [37] S. N. Shirodkar and U. V. Waghmare, *Phys. Rev. Lett.* **112**, 157601 (2014).
- [38] R. Fei, W. Kang, and L. Yang, *Phys. Rev. Lett.* **117**, 097601 (2016).
- [39] W. Song, R. Fei, and L. Yang, *Phys. Rev. B* **96**, 235420 (2017).
- [40] C. Huang, Y. Du, H. Wu, H. Xiang, K. Deng, and E. Kan, *Phys. Rev. Lett.* **120**, 147601 (2018).
- [41] W. Ding, J. Zhu, Z. Wang, Y. Gao, D. Xiao, Y. Gu, Z. Zhang, and W. Zhu, *Nat. Commun.* **8**, 14956 (2017).
- [42] F. Liu, L. You, K. L. Seyler, X. Li, P. Yu, J. Lin, X. Wang, J. Zhou, H. Wang, H. He, S. T. Pantelides, W. Zhou, P. Sharma, X. Xu, P. M. Ajayan, J. Wang, and Z. Liu, *Nat. Commun.* **7**, 12357 (2016).
- [43] K. Chang, J. Liu, H. Lin, N. Wang, K. Zhao, A. Zhang, F. Jin, Y. Zhong, X. Hu, W. Duan, Q. Zhang, L. Fu, Q.-K. Xue, X. Chen, and S.-H. Ji, *Science* **353**, 274 (2016).
- [44] Y. Zhou, D. Wu, Y. Zhu, Y. Cho, Q. He, X. Yang, K. Herrera, Z. Chu, Y. Han, M. C. Downer, H. Peng, and K. Lai, *Nano Lett.* **17**, 5508 (2017).
- [45] C. Cui, W.-J. Hu, X. Yan, C. Addiego, W. Gao, Y. Wang, Z. Wang, L. Li, Y. Cheng, P. Li, X. Zhang, H. N. Alshareef, T. Wu, W. Zhu, X. Pan, and L.-J. Li, *Nano Lett.* **18**, 1253 (2018).
- [46] S. M. Poh, S. J. R. Tan, H. Wang, P. Song, I. H. Abidi, X. Zhao, J. Dan, J. Chen, Z. Luo, S. J. Pennycook, A. H. Castro Neto, and K. P. Loh, *Nano Lett.* **18**, 6340 (2018).
- [47] S. Wan, Y. Li, W. Li, X. Mao, W. Zhu, and H. Zeng, *Nanoscale* **10**, 14885 (2018).
- [48] J. Xiao, H. Zhu, Y. Wang, W. Feng, Y. Hu, A. Dasgupta, Y. Han, Y. Wang, D. A. Muller, L. W. Martin, P. A. Hu, and X. Zhang, *Phys. Rev. Lett.* **120**, 227601 (2018).
- [49] C. Gong, E. M. Kim, Y. Wang, G. Lee, and X. Zhang, *Nat. Commun.* **10**, 2657 (2019).
- [50] W. Sun, W. Wang, D. Chen, Z. Cheng, and Y. Wang, *Nanoscale* **11**, 9931 (2019).
- [51] Y. Zhao, J.-J. Zhang, S. Yuan, and Z. Chen, *Adv. Funct. Mater.* **29**, 1901420 (2019).
- [52] P. E. Blöchl, *Phys. Rev. B* **50**, 17953 (1994).
- [53] G. Kresse and D. Joubert, *Phys. Rev. B* **59**, 1758 (1999).
- [54] G. Kresse and J. Furthmüller, *Phys. Rev. B* **54**, 11169 (1996).
- [55] G. Kresse and J. Furthmüller, *Comput. Mater. Sci.* **6**, 15 (1996).
- [56] J. P. Perdew, K. Burke, and M. Ernzerhof, *Phys. Rev. Lett.* **77**, 3865 (1996).
- [57] S. L. Dudarev, G. A. Botton, S. Y. Savrasov, C. J. Humphreys, and A. P. Sutton, *Phys. Rev. B* **57**, 1505 (1998).
- [58] S. Grimme, J. Antony, S. Ehrlich, and H. Krieg, *J. Chem. Phys.* **132**, 154104 (2010).
- [59] S. Grimme, S. Ehrlich, and L. Goerigk, *J. Comput. Chem.* **32**, 1456 (2011).
- [60] J. G. Yan Gong, J. Li, K. Zhu, M. Liao, X. Liu, Q. Zhang, L. Gu, L. Tang, X. Feng, D. Zhang, W. Li, C. Song, L. Wang, P. Yu, X. Chen, Y. Wang, H. Yao, W. Duan, Y. Xu, S.-C. Zhang *et al.*, *Chin. Phys. Lett.* **36**, 76801 (2019).
- [61] F. Xue, Y. Hou, Z. Wang, and R. Wu, *Phys. Rev. B* **100**, 224429 (2019).
- [62] X. Wang, R. Wu, D.-s. Wang, and A. J. Freeman, *Phys. Rev. B* **54**, 61 (1996).
- [63] J. Hu and R. Wu, *Phys. Rev. Lett.* **110**, 097202 (2013).
- [64] See Supplemental Material at <http://link.aps.org/supplemental/10.1103/PhysRevB.101.184426> for more details on the magnetic configurations, band alignments, band structures, and Chern number calculations.
- [65] S. V. Maleev, *Zh. Eksp. Teor. Fiz.* **70**, 2374 (1976) [*JETP* **43**, 1240 (1976)].
- [66] D. P. Pappas, K. P. Kämper, and H. Hopster, *Phys. Rev. Lett.* **64**, 3179 (1990).
- [67] K. De'Bell, A. B. MacIsaac, and J. P. Whitehead, *Rev. Mod. Phys.* **72**, 225 (2000).
- [68] S. T. Chui, *Phys. Rev. B* **50**, 12559 (1994).
- [69] A. B. MacIsaac, K. De'Bell, and J. P. Whitehead, *Phys. Rev. Lett.* **80**, 616 (1998).
- [70] A. Hucht, A. Moschel, and K. D. Usadel, *J. Magn. Magn. Mater.* **148**, 32 (1995).
- [71] A. B. MacIsaac, *Phys. A (Amsterdam, Neth.)* **239**, 147 (1997).
- [72] S. T. Chui, *Phys. Rev. Lett.* **74**, 3896 (1995).
- [73] L. Ying, C. Nanxian, Z. Hongmin, and W. Chengwen, *Solid State Commun.* **126**, 223 (2003).
- [74] J. Heyd, G. E. Scuseria, and M. Ernzerhof, *J. Chem. Phys.* **124**, 219906 (2006).